The definitive publisher version is available online at 10.1016/j.solmat.2023.112436

Enhanced solar-driven water splitting performance using oxygen vacancy rich ZnO photoanodes

Amar K. Salih, Matthew R. Phillips, Cuong Ton-That*

School of Mathematical and Physical Sciences, University of Technology Sydney, Ultimo, New South Wales 2007, Australia

*Corresponding author. E-mail address: Cuong.Ton-That@uts.edu.au

Abstract

This work reports a facile two-step method of producing highly efficient ZnO photoanodes for photoelectrochemical (PEC) water splitting under solar light conditions and describes the role of surface oxygen vacancies (V_O) in their enhanced PEC performance. The photoanode fabrication involves post-growth oxidation of a metallic Zn layer, which produces a nanostructured ZnO film consisting of ~50 nm diameter nanorods containing a high concentration of V_O defects. The PEC activity of the ZnO films is investigated by studying water oxidation in an aqueous electrolyte under simulated solar illumination. The relationship of PEC and charge transfer characteristics of the ZnO photoanodes with ionized surface V_O defects is established using cathodoluminescence, X-ray photoemission, voltammetry, electrochemical impedance spectroscopy and chronoamperometry. The combined results show that the photoanode fabricated in this work possesses a high surface density of ionized V_O states that facilitate the effective transportation of holes for water oxidation. It is found that the photoanode exhibits an exceptional photocurrent density of 1.14 mA/cm^2 at 1.23 V_{RHE}, being one of the best performances reported in the literature for ZnO-based photoelectrodes so far. Our results demonstrate a simple, low-cost method for fabricating highly efficient V_O rich ZnO-based PEC photoanodes that is suitable for large scale production.

Keywords: photoelectrochemical water splitting; oxides; photoanodes; surface defects; oxygen vacancies

1. Introduction

Utilizing renewable energy from hydrogen sources is currently attracting considerable attention to address energy and environmental issues. Photoelectrochemical (PEC) water splitting is widely considered to be a viable technique to generate sustainable, clean and storable hydrogen energy from water using solar radiation.[1-3] During water slitting, two separate half-reactions are involved in the PEC redox process: a water reduction reaction ($\mathrm{H_2}$ reduction, $\mathrm{2H_2O + 2e^- \rightarrow H_2 + 2OH^-}$) and a water oxidation reaction ($\mathrm{O_2}$ production, $\mathrm{2H_2O + 4h^+ \rightarrow O_2 + 4H^+}$).[3] When an n-type ZnO photoanode is immersed in a suitable water-based electrolyte, conduction band (CB) electrons flow from the ZnO electrode to the solution since the ZnO Fermi level is above the electrolyte redox potential. This outward flow of electrons to the electrolyte creates a depletion layer at the ZnO photoanode surface with a build-in potential and an associated electric field pointing towards redox interface that causes upward bending of the near-surface band edges.[4, 5] Under solar illumination, e-h pairs generated within the surface depletion layer by photoionization are formed and subsequently charge separated by the electric field. Consequently, photogenerated holes drift towards the semiconductor/electrolyte interface, where they oxidize water molecules creating O_2, while photogenerated electrons are transported to the cathode through an external bias voltage to reduce water molecules generating H_2.[6] Of these two-half reactions, the water oxidation process is considered to be a bottleneck in the PEC water splitting efficiency because it is a sluggish reaction requiring the rapid transfer of four holes to the electrolyte to create one molecule of oxygen. In comparison, the water reduction needs the transfer of a single electron to generate a molecule of hydrogen.

Several metal oxides such as Fe_2O_3, CdO, TiO_2, and ZnO have been evaluated as potential photoanodes for PEC water splitting because of their low fabrication cost and high stability in aqueous media compared with other types of traditional semiconductors.[1, 7-9] However, to date most of most metal oxide photoanodes have been proven to be unsuitable for

PEC applications. For example, hematite (α-Fe_2O_3) exhibits poor charge separation in its surface depletion layer due to a low hole drift mobility and short hole diffusion length,[10] CdO is not suitable as Cd is highly toxic while TiO_2 absorbs solar radiation poorly due to its wide bandgap and poor hole transport.[11] In contrast, ZnO is an attractive PEC candidate due to its favorable band edge energy positions with respect to the redox potentials of water, low toxicity, ability to be grown in a variety of bespoke nanostructures, and significantly larger hole mobility compared with TiO_2 and Fe_2O_3.[12-14] Recently, it has been reported that the introduction of oxygen vacancy (V_O) defects can be used to increase the PEC efficiency of oxide-based photoanodes.[15-18]. Different methods have been attempted to create V_O defects in ZnO, including hydrogenation, growth under oxygen-deficient conditions, post-growth annealing under a reducing atmosphere, as well as lowering the V_O formation energy by the incorporation of acceptor dopants.[19-22] Significantly, Duan *et al.*[17] used electrochemical reduction to increase the V_O density in ZnO and observed a threefold increase in the PEC photocurrent density. While the benefits of V_O incorporation into oxide photoanodes on the PEC performance are clear,[1] no phenomenological model currently exists to explain the role of this defect in the underlying electrical processes at metal oxide photoanodes. This work focuses on the incorporation of V_O defects in ZnO photoanodes by the oxidation of metallic Zn films and their role in mediating the PEC performance. It is found that V_O rich ZnO photoanodes fabricated using this approach exhibit an exceptional photocurrent density of 1.14 mA/cm^2 at 1.23 V_{RHE}, being among the best ZnO-based PEC performance values reported in the literature so far. These ZnO photoanodes exhibit an intense signature green luminescence (GL) band associated with V_O defects. Accordingly, we present a model that explains the relationship between the density of V_O defects in ZnO photoanodes and their PEC activity, shown in the schematic in Figure 1. Here, *e*-*h* pairs are separated by the electric field across the depletion layer efficiently transporting holes to the ZnO photoanode/electrolyte interface rich in reactive charged V_O^{2+}

surface sites that enhance the PEC water redox reaction. The high concentration of near interface V_O^{2+} is produced by the transformation of bulk V_O^0 due to the surface upward bending of the $V_O^{2+/0}$ charge transfer level (CTL) above the Fermi level of the *n*-type ZnO photoanode. The model is supported by cathodoluminescence (CL) and X-ray photoemission spectroscopy (XPS) studies, which both confirm that the ZnO photoanode with the highest PEC performance has the largest V_O concentration. We further present a facile, inexpensive method for producing high-performance ZnO-based photoanodes that exhibit a high absorption efficiency in the visible spectral range and low charge-transfer resistance.

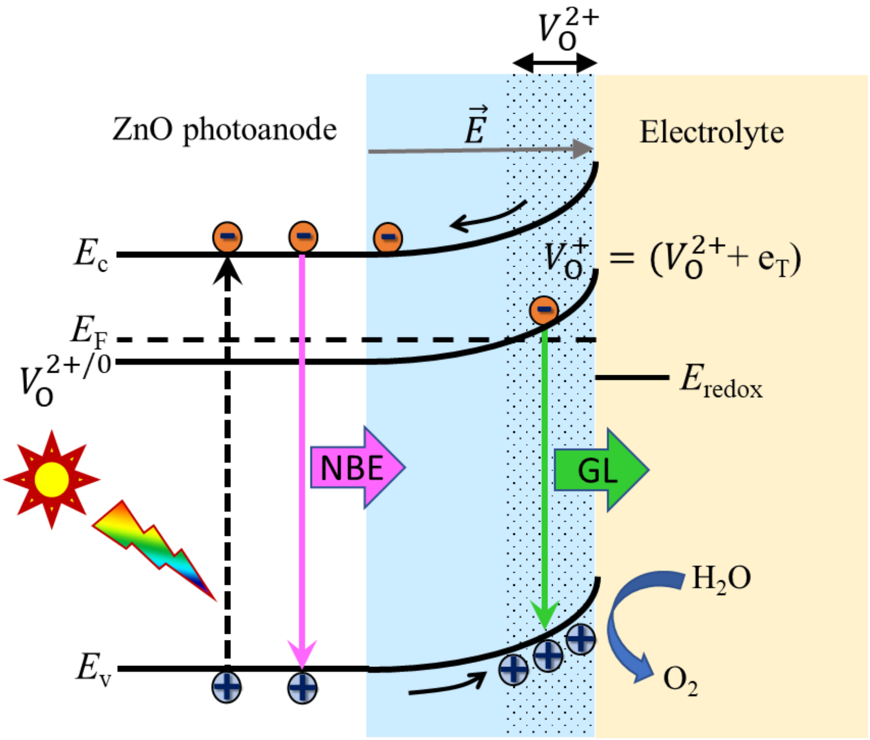

Figure 1. A schematic representation of the PEC and GL processes in a V_O rich ZnO photoanode. Since the surface pinned Fermi level (E_F) of the *n*-type ZnO photoanode is typically above the electrolyte redox potential (E_{redox}), CB electrons flow from ZnO to the electrolyte. This charge equalization produces a surface depletion layer (blue region) with an associated outward pointing electric field that causes upward bending of the band edges. The *e-h* pairs photoexcited within the depletion layer are charge separated by the electric field, which transports holes

(electrons) to the photoanode (cathode)/electrolyte interface to drive the oxidation (reduction) reaction. Notably, the $V_{\mathrm{O}}^{2+/0}$ CTL also bends upwards and when it rises above E_{F} a near surface layer of reactive V_{O}^{2+} defects (blue shaded region) is produced that promotes the PEC water redox process. The V_{O}^{2+}defects can also capture a free electron forming the V_{O}^{+} (V_{O}^{2+}+ e_T) state with a deeply trapped electron (e_T) that can radiatively recombine with a photogenerated free hole, producing the observed GL (green arrow) and restoring the V_{O}^{2+} state.[23] Ultraviolet emission (purple arrow) arises from the near-band-edge (NBE) *e-h* recombination in the ZnO bulk.

2. Experimental

2.1 Fabrication of ZnO thin films for photoanodes

Two fabrication approaches were used to produce ZnO photoanodes. The first approach involved depositing a metallic Zn film of ~ 200 nm on an FTO-coated glass substrate (Sigma-Aldrich, 8 Ω/sq resistivity) using a DC sputtering system (NSC-4000, Nanomaster). The sputtering target was metallic Zn (99.995 % purity, ACI alloys Inc.). The sputtering chamber had a base pressure of 8×10^{-6} torr and was maintained at a working pressure of 3×10^{-3} torr during film deposition at a DC sputtering power of 100 W, a constant Ar flow of 75 sccm for 10 mins. The deposited Zn films were oxidized in ambient air using a tube furnace at 450, 550, and 650 $^{\mathrm{o}}$C (denoted as Zn-450$^{\mathrm{o}}$C, Zn-550$^{\mathrm{o}}$C, and Zn-650$^{\mathrm{o}}$C, respectively). The furnace was heated at a rate of 10 °C/min to the set temperature and the films were annealed for two hours. The second approach was to deposit a ZnO film via DC reactive sputtering deposition in a 1:1 Ar/O_2 gas mixture. The film was then annealed for 2 hours at 550 $^{\mathrm{o}}$C separately in argon or air atmosphere (denoted as ZnO-argon, and ZnO-air, respectively, and ZnO-AG for as-grown ZnO). It is worth noting that the fabricated ZnO photoanodes will exhibit upward surface bending of the band edges due to chemisorbed oxygen species depleting electrons from the ZnO surface.

2.2 Structural and optical characterization

The fabricated ZnO films were characterized using a broad variety of complementary analytical techniques. First, the crystallinity of the ZnO films was examined using X-ray diffraction (XRD, Rigaku Miniflex-600) using Cu Kα radiation $\lambda = 1.5406$ Å. The ZnO film morphologies were investigated using Zeiss Supra 55VP scanning electron microscope (SEM). The optical properties of the films were studied using a double-beam UV-Vis spectrometer (Jasco V-570). CL measurements were performed on a FEI Quanta 200 SEM equipped with a parabolic mirror collector and an Ocean Optics QE65000 spectrometer; all CL spectra were corrected for the total system response. Chemical state analysis of the films was conducted using XPS (ESCALAB250Xi, Thermo Fisher); binding energies were calibrated using the C 1*s* peak at 286 eV. All samples were etched with Ar^+ ions for 30 seconds before XPS analysis.

2.3 Photoelectrochemical and photocatalytic measurements

The PEC performance of the ZnO photoanodes was investigated using chronoamperometry, linear sweep voltammetry, and electrochemical impedance spectroscopy in a quartz cell connected to a Voltalab PGZ 402 potentiostat via a three-electrode measuring setup as described previously.[24] ZnO thin-films, saturated calomel electrode (SCE), and platinum coil were used as working electrodes, reference electrode, and counter electrode, respectively. The measured potential (V_{SCE}) was converted to the reversible hydrogen electrode (V_{RHE}) potential using Nernst equation:[25]

$$V_{RHE} = V_{SCE} + 0.0591 \times pH + V^0_{SCE} \qquad \text{Eq. (1)}$$

where V_{SCE} is the applied potential versus the SCE, and V^0_{SCE} (= 0.244 V) is the standard redox potential of the SCE at 298 K. A 0.5 M Na_2SO_4 solution was utilized as an electrolyte. The photocatalytic activity of the ZnO photoanode was assessed under simulated solar light irradiation using a Xenon lamp (Max-303, 300 W) with a light intensity of 100 mW/cm^2 in the wavelength range of 300 – 600 nm The charge transfer resistance (R_{ct}) of the deposited films was determined using electrochemical impedance spectroscopy (EIS) in the dark and under illumination. The EIS measurements were made over the frequency range from 10 mHz to 100 kHz.

3. Results and discussion

3.1 Fabrication of ZnO photoanodes rich with oxygen vacancies

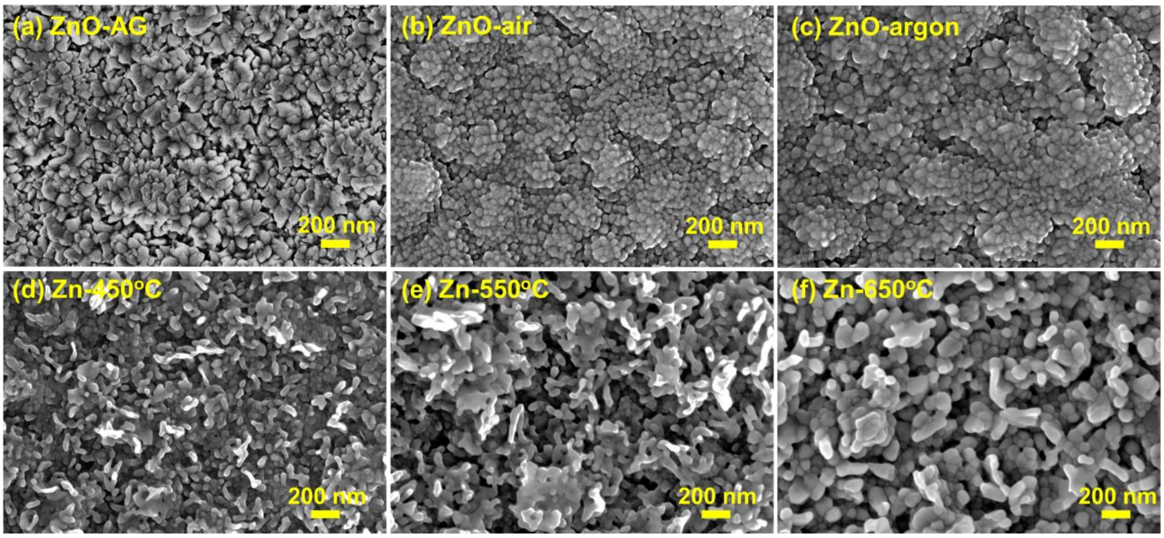

Figure 2. Typical SEM images of the ZnO films (a, b, and c) and the oxidized Zn films (d, e and f). The ZnO films grow in the form of closely packed crystal grains, while the oxidized Zn films are comprised of randomly oriented nanorods. The nanorods in the oxidized Zn films become larger in both diameter and length as the post-oxidation temperature is raised from 450 to 650^{o}C.

Typical SEM images of the ZnO films studied are displayed in Figure 2. The ZnO-AG film is comprised of plate-like nanostructures, the platelets are ~ 100 nm in lateral dimensions as seen in Figure 2(a). The morphology and surface features of the ZnO film prior to annealing are analogous to those of the FTO substrate (see the SEM image of the bare FTO glass in Supplementary Material Figure S1), suggesting that the surface structure of the FTO glass substrate is responsible for the observed rough morphology and voids in the ZnO-AG film. The annealed ZnO-air and ZnO-argon films have a granular texture consisting of densely packed grains with a lateral size of ~ 50 nm, as shown in Figure 2(b, c). The morphology of the oxidized Zn films is clearly different and comprises of randomly oriented ZnO nanorods with a ~ 20 nm diameter (see Figure S2 for image analysis of these rod-like structures.) The nanorods are formed during the annealing process as a result of interaction between the metallic Zn layer and oxygen, and are found to enlarge with increasing annealing temperature. These results are significant as the active surface area of a ZnO photoanode is directly proportional to its PEC activity.

The XRD patterns for both the ZnO and oxidized Zn film sets are shown in Figure 3. All the diffraction patterns contain peaks (indicated by red dots) corresponding to the FTO coating layer of the substrate. The annealed ZnO films (ZnO-argon and ZnO-air) exhibit a strong (0002) XRD peak, indicating that these films possess wurtzite crystalline structure with a preferential *c*-axis orientation. On the other hand, the ZnO-AG film is poorly crystalline, its ZnO XRD (0002) peak is considerably weaker than the FTO peak at $2\theta \approx 34^o$ and cannot be distinguished clearly due to their strong overlap. However, the broadening of the ZnO-AG XRD line at ~ 34^o on the high 2θ side of the peak is consistent with the presence of a weak ZnO (0002) reflection. Since the ZnO-AG film is not highly crystalline, its XRD (0002) peak is considerably weaker than the FTO peak and thus cannot be distinguished clearly; this is in contrast to those of the annealed crystalline films shown in the same figure. However, the broadening of the ZnO-AG XRD peak at ~ 35^o towards to the high 2θ value is consistent with the presence of a weak (0002) peak.The (0002) diffraction peak is weak in the ZnO-AG and enhanced substantially after annealing as the film crystallinity improves. For the oxidized Zn films (Zn-450^{o}C, Zn-550^{o}C, and Zn-650^{o}C), multiple diffraction peaks are observed and can be indexed to (11-20), (0002), (10-11), (10-12), (11-20), (10-13), and (11-22) planes of wurtzite ZnO since their XRD patterns are governed by the growth of crystalline nanorods along random directions on the substrate (see Figure 2). These XRD findings are consistent with the compositional and chemical state analysis results by XPS for both the ZnO and oxidized Zn film sets shown in Figure S3, which confirms the successful conversion of the metallic Zn films to highly crystalline ZnO by oxidative annealing. The Zn-650^{o}C film displays only slight improvement in its crystallinity compared with Zn-450^{o}C and Zn-550^{o}C.

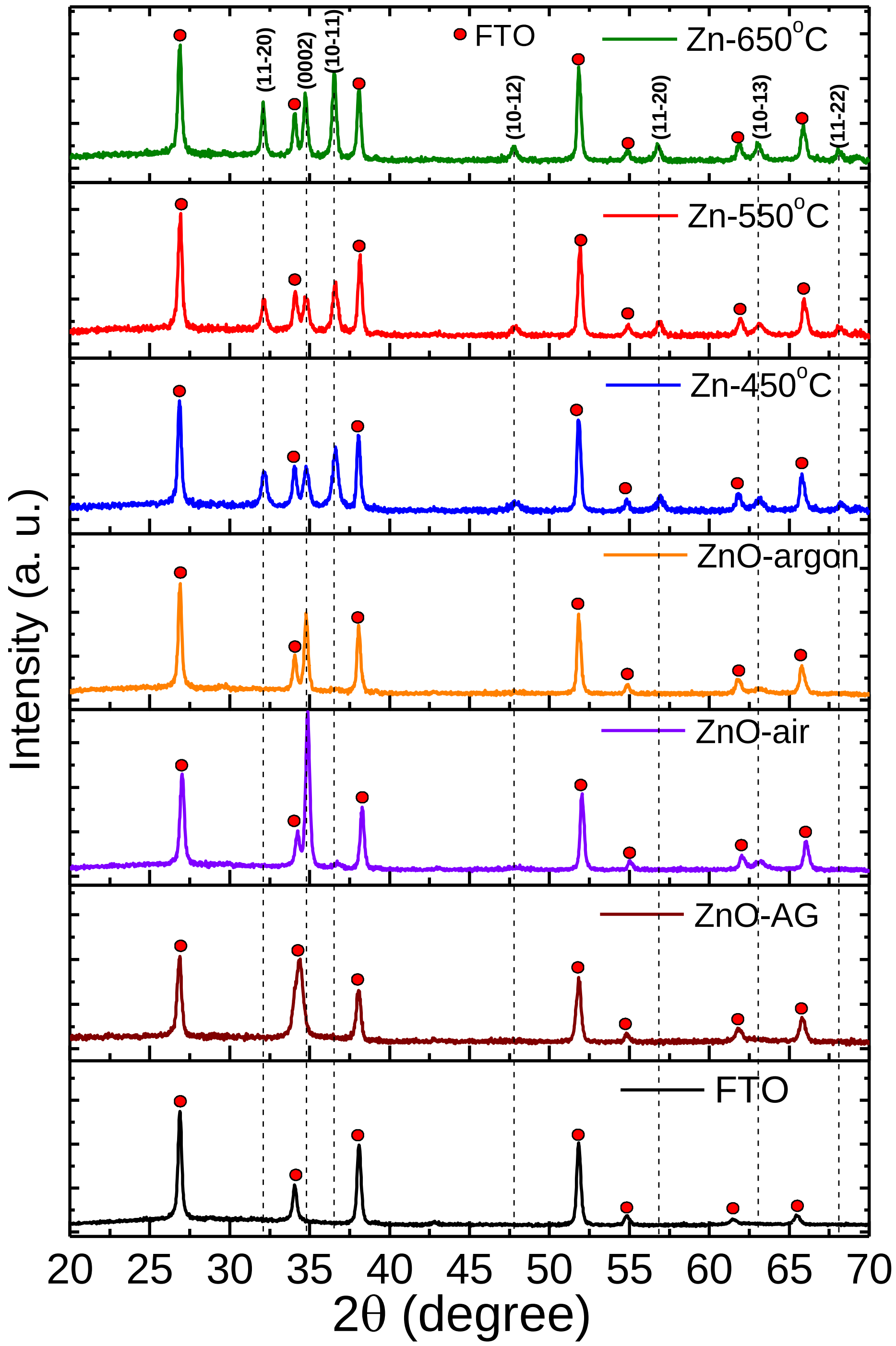

Figure 3. XRD patterns for the oxidized Zn and ZnO films. The peaks are indexed as follows: the red dots correspond to the FTO substrate while the dashed lines indicate reflections from the ZnO films. All the ZnO peaks can be identified as the wurzite phase of ZnO, indicating the

successful conversion of the metallic Zn films (Zn-450^{o}C, Zn-550^{o}C and Zn-650^{o}C) to highly crystalline ZnO by oxidative annealing. The oxidized Zn films comprises of crystallites with multiple orientations such as (0002), (11-20), (10-11) and (11-20), while the ZnO films (ZnO-AG, ZnO-argon, and ZnO-air) have a predominantly (0002) growth orientation.

The optical properties of the ZnO films are determined using UV-Vis spectrometry [Figure 4(a, b)]. The ZnO films exhibit absorption only in the UV spectral region with a sharp absorption edge at 387 ± 3 nm (3.24 ± 0.02 eV from the Tauc plot extrapolation), close to the bandgap of bulk ZnO, while the optical absorption spectra of the oxidized Zn films display an exponential absorption edge over the visible spectral range. The extended absorption tails in the spectra of the Zn-450^{o}C, Zn-550^{o}C, and Zn-650^{o}C films can be attributed to light scattering in the nanostructured films and the Urbach tail effect [26] caused by band edge potential fluctuations produced by a high density of V_{O} defects. The light scattering effect in these films could be significant since the size of the nanorods is of the order of the wavelength of visible light. From the Tauc plot, the bandgap of these oxidized Zn films can be determined to be 3.01 ± 0.02 eV, which is significantly narrower than that of the ZnO films. The narrowed bandgap together with the exponential absorption edge enable these films to expand the absorption range thus enhances the PEC activity in the visible region.

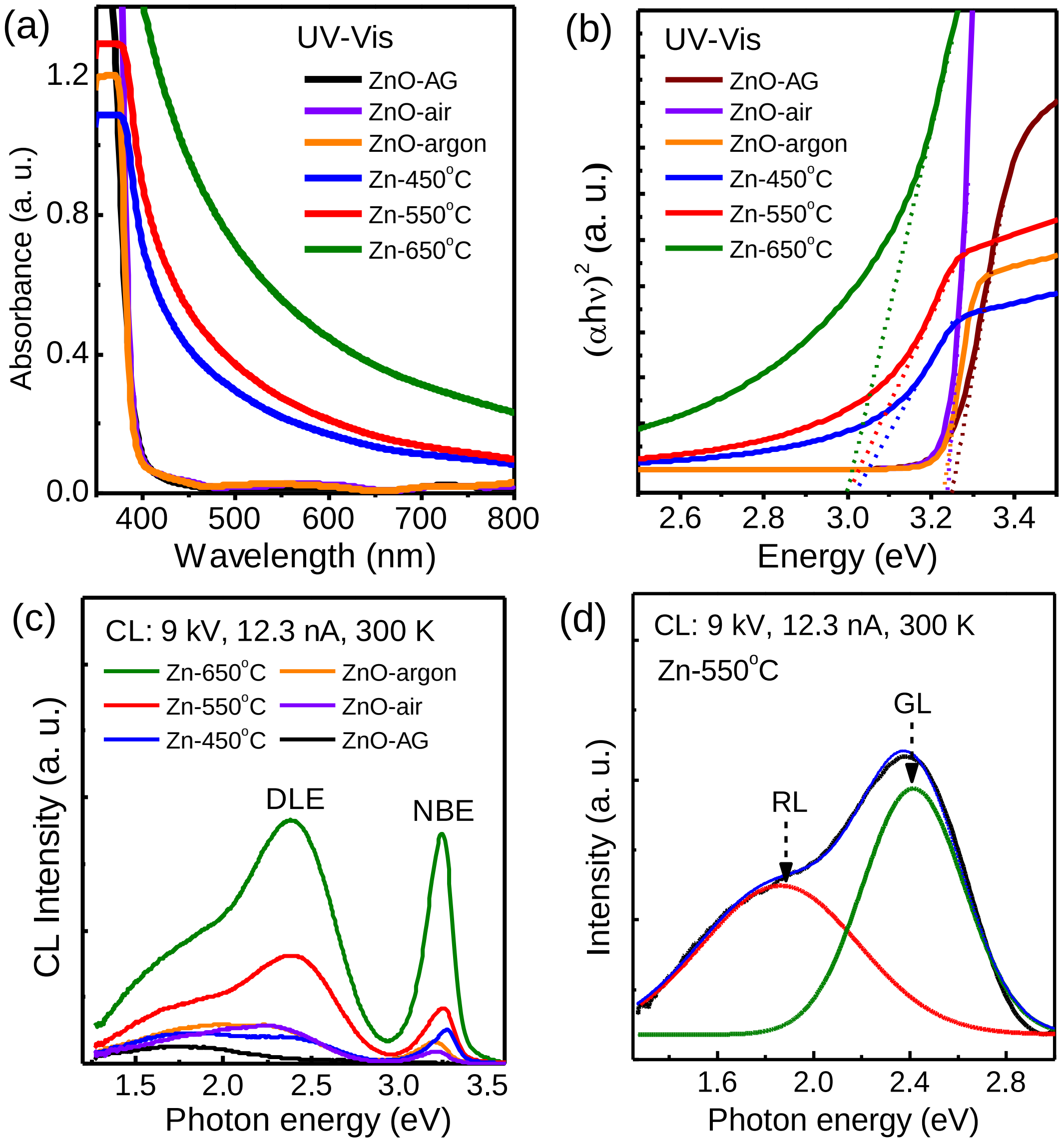

Figure 4. (a) UV-Vis absorption spectra measured from the as-grown and thermally annealed ZnO and oxidized Zn films at 450°C, 550°C and 650°C. The ZnO films exhibit a sharp optical absorption edge at 402 nm. In contrast, the spectra from the oxidized Zn films display an exponential absorption tail due to the presence of a high concentration of V_O defects. (b) Tauc plots for the films, yielding $E_g = 3.24 \pm 0.02$ eV and 3.01 ± 0.02 eV for the ZnO and oxidized Zn films, respectively. (c) CL spectra of the ZnO and oxidized Zn films acquired under identical conditions (300 K, 9 kV and 12.3 nA). The ZnO-AG film exhibits only a RL peak at 1.9 eV. Conversely, the other films exhibit three emission bands: UV at 3.3 eV, GL at 2.45 eV and RL at ~1.9 eV, attributed to NBE *e-h* recombination, V_O and V_{Zn}, respectively. (d) Gaussian fits of the deep-level emission for the oxidized Zn-550°C film. The Zn-550°C spectrum has the largest I_{GL}/I_{NBE} ratio (see Table S1), indicating that this film has the highest V_O density.

The defect structure in both the ZnO and oxidized Zn film sets is further studied using CL spectroscopy [Figure 4(c, d)]. All the films, except the ZnO-AG, exhibit a characteristic NBE emission at ~ 3.3 eV due to the radiative recombination of free excitons in wurtzite ZnO.[27] The NBE emission is accompanied by a deep-level emission (DLE) comprised of a GL peak centred at 2.45 eV and a red luminescence (RL) shoulder at ~1.80 eV; these luminescence bands have previously been assigned to V_{O} and V_{Zn} defects, respectively.[28, 29] The ZnO-AG film displays only the RL and no NBE emission, indicating that this film contains an excess of V_{Zn} defects consistent with the oxygen-rich growth environment. The ZnO-air and ZnO-argon CL spectra show the presence of an NBE emission as defects are gradually annealed out. For the oxidized Zn films, the strong green emission indicates an abundance of V_{O} defects, which improves their light absorption capability as observed in the UV-Vis results. The strong GL emission observed in the oxidized Zn films confirms a high density of V_{O}. In wurtzite ZnO, V_{O} has three possible charge states: neutral V_{O}^{0}, singly ionized V_{O}^{+} and doubly ionized V_{O}^{2+}. Computational studies indicate that V_{O}^{+} exhibits negative U behavior and is unstable under thermal equilibrium.[30] Accordingly, V_{O}^{+} instantly transforms into its V_{O}^{0} or V_{O}^{2+} charge state by the gain or loss of an electron, depending on whether the ZnO Fermi level is above or below the $V_{\mathrm{O}}^{2+/0}$ CTL, respectively (see Figure 1). However, V_{O}^{0} is the thermodynamically stable charge state in the ZnO bulk due to its *n*-type nature with the Fermi level above the CTL. Conversely, V_{O}^{2+} states exist within the near surface region of the depletion layer due to the $V_{\mathrm{O}}^{2+/0}$ CTL bending above the ZnO Fermi level. In addition, it is widely reported that the ionized V_{O} signature GL emission intensity is strongest at the surface of ZnO nanowires.[31, 32] As a result, the measured GL emission in Figure 4(c) results from radiative recombination involving V_{O} defects. Here, a surface V_{O}^{2+} defect captures a free electron and converts into a V_{O}^{+} state with a deeply trapped electron that radiatively recombines with a photogenerated hole in the valence band, restoring the V_{O}^{2+} center and producing the GL (see Figure 1).[16, 23, 28, 33] Notably, the overall CL intensity of the oxidized Zn films increases with increasing annealing temperature as expected due to the improvement in film crystallinity and the associated removal of non-radiative defects, consistent with the XRD results as shown above. The DLE band is fitted with two Gaussian components to find the integrated intensities of the GL and RL bands for each of the ZnO photoanodes [Figure 4(d)]. The large variation of the GL and RL intensities in the ZnO films are evidenced in Table S1, which shows the $I_{\mathrm{GL}}/I_{\mathrm{NBE}}$ and $I_{\mathrm{RL}}/I_{\mathrm{NBE}}$ intensity ratios. The ZnO films process larger I_{RL} than I_{GL} as the formation of V_{Zn} is favourable in oxygen-rich growth conditions. On the other hand, the GL is the dominate peak in the oxidized Zn films with the Zn-550$^{\mathrm{o}}$C film exhibiting the largest $I_{\mathrm{GL}}/I_{\mathrm{NBE}}$ ratio, which renders this film with its high V_{O} density suitable for PEC water oxidation. These CL point defect characterization findings are further supported by the oxidation state XPS analysis shown in Figure S2. As displayed in this figure, the O 1s spectra for the films can be deconvoluted into two peaks at 530.6 eV, which corresponds to O^{2-} ions in the wurtzite fully coordinated ZnO, and at 532.3 eV ascribed to O^{2-} ions with a V_{O} defect nearby.[34] The relative oxygen vacancy concentrations present in the films are estimated by obtaining the intensity ratio of the two deconvoluted peaks; this ratio is found to be $I(V_{\mathrm{O}})/I(\mathrm{O\text{-}Zn}) = 0.28$, 0.30, and 0.37 (± 0.2) for ZnO-air, ZnO-argon and Zn-550$^{\mathrm{o}}$C films, respectively. This result further confirms that the Zn-550$^{\mathrm{o}}$C film has a higher V_{O} concentration compared to the as-grown ZnO films.

3.2 PEC water splitting performance

The PEC performance of the ZnO photoanodes over the potential range of 0 – 1.4 $\mathrm{V_{RHE}}$ is shown in Figure 5(a) and the measured photocurrent density, I_{photo}, at 1.23 $\mathrm{V_{RHE}}$ is presented in Table S1. The ZnO-AG films show the lowest photocurrent density of 0.07 mA/cm^2 at 1.23 $\mathrm{V_{RHE}}$ due to their low film quality, consistent with the CL result that shows their optical properties are dominated by defects. The photocatalytic activity increases slightly to 0.13 and 0.34 mA/cm^2 at 1.23 $\mathrm{V_{RHE}}$ when the ZnO-AG film is annealed at 550$^{\mathrm{o}}$C in air (ZnO-air) and argon (ZnO-argon), respectively. This PEC performance enhancement could be attributable to the improvement in the film crystallinity, and possibly a higher density of V_O defects as revealed by the CL [see Figure 4(c)]. In comparison, the oxidized Zn photoanodes exhibit a three- to four-fold increase over the ZnO counterparts; at 1.23 V_{RHE}, the Zn-450^{o}C and Zn-550^{o}C photoanodes have a photocurrent density of 0.87 and 1.14 mA/cm^2, respectively. As discussed above, this remarkable improvement can be attributed to several factors. First, the oxidized Zn photoanodes have a much higher concentration of near-surface charged V_O defects. These reactive centres are known to act as preferential active sites for the surface adsorption of reactive oxygen species, such as H_2O, H and O_2, with their bonding at the V_O sites facilitating efficient charge transfer in the PEC process.[17, 18] Second, the V_O rich oxidized Zn films have a narrower bandgap due to the Urbach tail effect generating an exponential absorption edge that extends into the visible spectral range, improving light absorption efficiency of the photoanode under solar light irradiation. Third, the oxidized Zn films are comprised of nanorods with a large surface area that significantly increases the interaction between the electrolyte and ZnO photoanode. Notably, the oxidized Zn-650^{o}C film has a lower photocurrent of 0.72 mA/cm^2 at 1.23 V_{RHE}. Annealing FTO-coated glass at temperatures above 600 ^{o}C has been shown to cause a reduction in its electrical conductivity due to the diffusion of Sn from the FTO coating [35, 36]; the lower photocurrent in the Zn-650^{o}C photoanode can therefore be attributed to thermal damage to the FTO substrate.

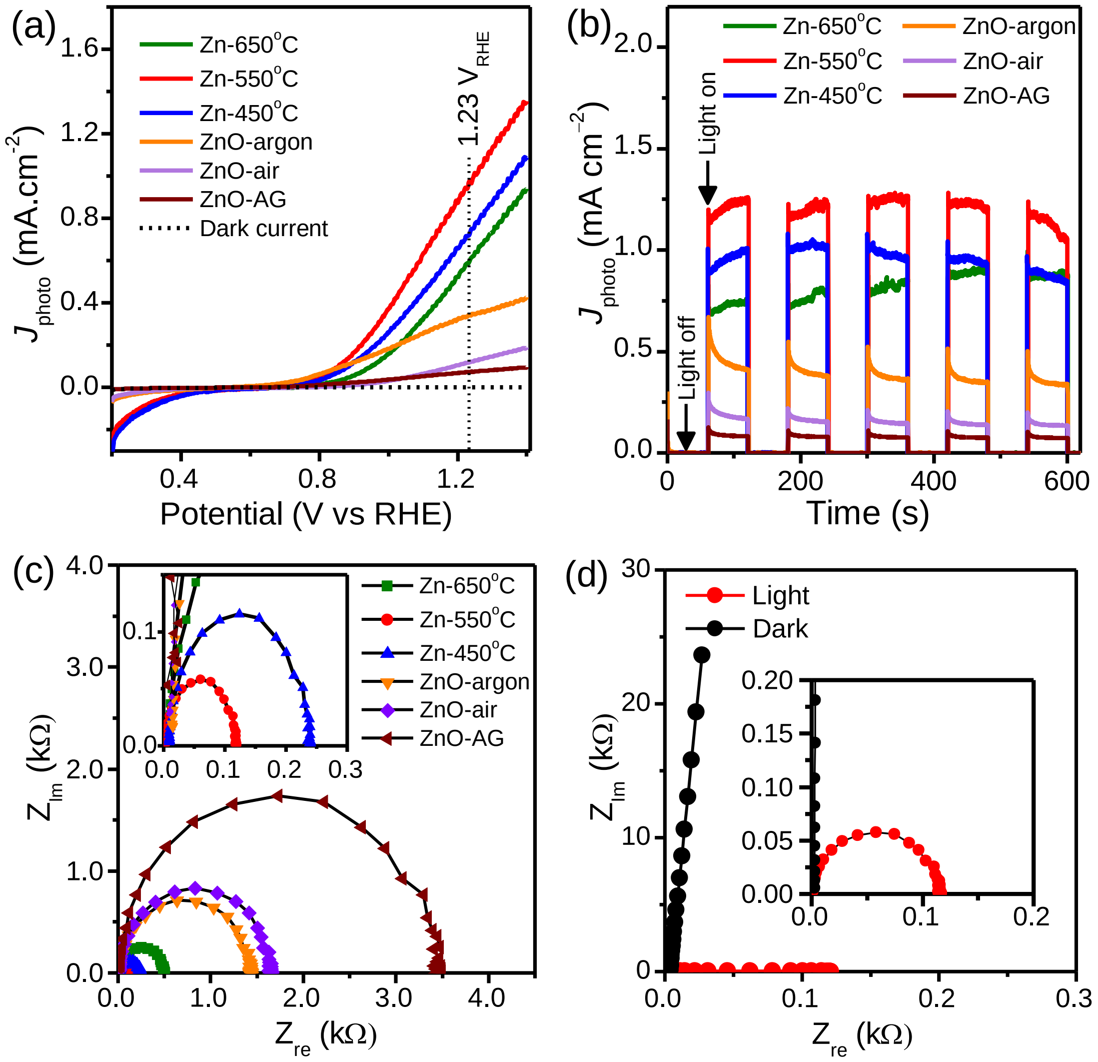

Figure 5. (a) Linear sweep voltammetry (LSV) plots, (b) chopped light chronoamperometry curves, and (c) Nyquist plots from impedance spectroscopy measurements for the ZnO and oxidized Zn photoanodes in 0.5M Na_2SO_4 aqueous solution and under 100 mW/cm^2 light intensity. The oxidized Zn photoanodes show a higher photocurrent density and lower charge transfer resistance, R_{ct}, compared with the ZnO counterparts. (d) Impedance spectroscopy of the Zn-550°C photoanode in the dark and under 1.23 V_{RHE} illumination. The resistance is extremely large in the dark, confirming that the photocurrent is generated by photogenerated *e*-*h* pairs induced by solar irradiation.

A chopped light chronoamperometry test reveals a similar photoactivity trend at 1.23 V_{RHE} under AM 1.5G solar simulator irradiation. Figure 5(b) shows the photocurrent density J_{photo} versus time under on/off solar irradiation. In the absence of solar irradiation, all the photoanodes do not produce a measurable photocurrent. When the photoanode is illuminated, a large number of charge separated photoexcited carriers accumulate at the photoanode/electrolyte interface, resulting in the instantaneous generation of photocurrent spikes. Notably the Zn-550°C photoanode with the highest J_{photo} also contains the highest V_O density. With the annealed ZnO photoanodes, an exponential drop in photocurrent is observed with increasing light exposure time which is repeated after blanking the optical excitation cycle as shown in Figure 5(b). This decrease in the photocurrent could arise from shallow defects trapping the charge separated carriers producing an opposing electric field that screens the in-built surface field. In contrast, with the Zn-450°C, Zn-550°C, and Zn-650°C photoanodes, following light exposure after the initial spike, the photocurrent slowly increases, saturates and maintains its intensity at re-exposure after most light-off cycles. These time dependent photocurrent kinetics are likely caused by the high density of ionized V_O defects being effective centers for carrier trapping and de-trapping, preventing free holes reaching the surface of the photoanode until a steady state condition is achieved.[37, 38]

The kinetics of the PEC process at the ZnO photoanode/electrolyte interface was assessed using the EIS technique at 1.23 V_{RHE} under 100 mW/cm^2 light intensity and the Nyquist plots for the six photoanodes are shown in Figure 5(c). The semicircle diameter of the Nyquist plot represents the charge transfer resistance (R_{ct}), which is shown in Table S1 for both the ZnO and oxidized Zn photoanodes. For the ZnO-AG photoanode, the plot is an incomplete semicircle, indicating a very large R_{ct} value. While with the annealed ZnO samples R_{ct} = 1.66 and 1.42 kΩ for the ZnO-air and ZnO-argon photoanodes, respectively. In comparison, the electrical impedance is an order of magnitude lower for the Zn-450°C, Zn-550°C, and Zn-650°C photoanodes with R_{ct} = 0.24, 0.12, and 0.50 kΩ, respectively. The relatively high R_{ct} for the Zn-650°C photoanodes is likely due to the thermal damage of the FTO substrate caused by the high annealing temperature. The remarkably high electrical conductivity of the Zn-550°C photoanode can be attributed to the high surface density of ionized V_O states, which creates a layer of holes at the photoanode/electrolyte interface as a result of the electric field across the depletion layer in the photoanode (see Figure 1). Moreover, the oxidized Zn films are comprised of randomly oriented nanorods with a large surface area that enhances its interaction with the electrolyte. The EIS of the Zn-550^{o}C sample was also measured both in the dark and under light exposure at 100 mW/cm^2 intensity [Figure 5(d)]. In the dark, the Nyquist plot is an incomplete semicircle and only a straight line is present due to very high resistance. This finding is consistent with the dark photocurrent exhibited in the LSV and chopped light chronoamperometry results [see Figure 5(a, b)], which confirms that the photocurrent is generated by photogenerated *e-h* pairs induced by solar irradiation and is not an electrochemical current. It also confirms the extremely high PEC activity of the Zn-550^{o}C photoanode.

3.3 Comparison with other ZnO photoanodes

The PEC performance of the optimized Zn film is compared with the reported results for ZnO photoanodes in the literature in Table 1. Comparison is made for photoanodes exposed to AM 1.5G sunlight and similar illumination conditions. As seen in the table, the Zn-550^{o}C film has a photocurrent density of 1.14 mA/cm^2 at 1.23V_{RHE}, which is higher than most previously reported for ZnO photoanodes in the literature. The superior performance of this film can be attributed to several factors. First, this film consists of randomly oriented nanorods, giving rise to a large interaction surface area with the electrolyte compared with the ZnO films fabricated by conventional sputtering or chemical vapor deposition (CVD) methods.[39-42] The high quality crystalline nanorods in the oxidized Zn film possess a high density of ionized V_O defects that facilitate the effective transportation of holes to the surface of the photoanode to oxidize the water. Second, the reduction in the ZnO bandgap to 3.0 eV achieved with the Zn oxidation method is significantly greater than that achieved in nanostructured ZnO thin films.[15, 43-48] Third, the oxidized Zn film exhibits an extended absorption tail in the visible spectral region produced by a high density of V_O defects. These structural and optical properties enable this film to capture a large fraction of the solar radiation.

Table 1. Comparison of ZnO photoanodes and their PEC performances reported in the literature. Compared to previous reports, the Zn-550°C photoanode has excellent PEC performance with J_{photo} = 1.14 mA/cm^2 at 1.23 V vs RHE. This photocurrent density is the largest among the ZnO photoanodes investigated to date, which include nanostructured thin films produced by physical, chemical and chemo-physical methods.

Fabrication method	**Photoanode structure**	**J_{photo} (mA/cm^2)**	**Bias voltage (V)**	**Electrolyte**	**Light source**	**Ref.**
Oxidation of Zn films	Nanorods	1.14	1.23	0.5 M Na_2SO_4	AM 1.5G (100 mW/cm^2)	This work
Hydrothermal	Nanorods	~1.30	1.23	0.5 M Na_2SO_4	AM 1.5G solar	[45]
Chemical synthesis	Nanorods	0.705	1.23	0.5 M Na_2SO_4	AM 1.5G (100 mW/cm^2)	[15]
Dip coating	Nanorods	0.39	1.23	0.5 M Na_2SO_4	Xe lamp (100 mW/cm^2)	[46]
Aerosol assisted CVD	Thin film	0.3	1.1	0.1 M Na_2SO_4	AM 1.5G solar	[41]
RF sputtering	Thin film	0.25	1.23	0.1 M KOH	150 W Xe lamp	[39]
Chemical bath deposition	Nanosheets	0.2	1.23	–	300 W Xe lamp (100 mW/cm^2)	[44]
Chemical bath deposition	Nanowires	~0.15	1.23	0.1 M NaOH	UV lamp (11.5 mW/cm^2)	[49]
MOCVD	Nanowires	0.11	1.23	0.35 M Na_2SO_3 + 0.25 M Na_2S	300 W Xe lamp	[50]
DC reactive sputtering	Thin film	0.05	1.23	0.5 M Na_2SO_4	AM 1.5G solar	[40]
Hydrothermal	Nanowires	0.03	1.23	0.1 M Na_2S + 0.2 M NaOH	500 W Xe lamp	[48]
Hydrothermal	Nanorods	~0.01	1.23	0.1 M NaOH	–	[47]
Sol-gel coating	Thin film	0.005	1.00	0.5 M Na_2CO_3	500 W Xe lamp	[42]

4. Conclusions

This study demonstrates a facile, inexpensive method for fabricating V_O-rich ZnO photoanodes with high PEC activity under solar light irradiation. The method involves post-growth oxidation of a metallic Zn film, which produces a ZnO film comprised of randomly oriented nanorods that contain a high concentration of V_O defects. These nanostructured ZnO films are well suited as PEC photoanodes in water splitting applications due to their large surface area, strong optical absorption in the visible spectral range and charge transfer characteristics. Compared with previous reports on ZnO photoanodes, our V_O-rich ZnO photoanodes exhibit outstanding PEC performance with an exceptional photocurrent density of 1.14 mA/cm^2 at 1.23 V_{RHE}. Using correlative characterization techniques, we establish a direct relationship between the density of charged V_O defects in the subsurface region of ZnO photoanodes and their PEC activity. Our results demonstrate that the PEC efficiency and electrical conductivity of ZnO photoanodes can be considerably enhanced by controlling the surface defect structure to increase the generation and charge transfer of photoexcited carriers.

CRediT authorship contribution statement

Amar K. Salih: Conceptualization, Investigation, Formal analysis, Writing – original draft. **Matthew R. Phillips:** Data curation, Writing – review & editing. **Cuong Ton-That:** Formal analysis, Supervision, Writing – review & editing

Declaration of Competing Interest

The authors declare that they have no known competing financial interests or personal relationships that could have appeared to influence the work reported in this paper.

Data availability

Data will be made available on request.

Acknowledgements

The authors acknowledge the technical assistance of Curtis Irvine, Herbert Yuan and Mark Lockrey. This work was supported under Australian Research Council (ARC) Discovery Project funding scheme (project DP210101146).

Appendix A. Supplementary material

Supplementary data to this article can be found online at xxx.

References

[1] S.M. Fawzy, M.M. Omar, N.K. Allam, Photoelectrochemical water splitting by defects in nanostructured multinary transition metal oxides, Solar Energy Materials and Solar Cells, 194 (2019) 184-194.

[2] M.D. Regulacio, M.-Y. Han, Multinary I-III-VI2 and I2-II-IV-VI4 semiconductor nanostructures for photocatalytic applications, Accounts of chemical research, 49 (2016) 511-519.

[3] M.G. Walter, E.L. Warren, J.R. McKone, S.W. Boettcher, Q. Mi, E.A. Santori, N.S. Lewis, Solar water splitting cells, Chemical reviews, 110 (2010) 6446-6473.

[4] M. Grätzel, Photoelectrochemical cells, Nature, 414 (2001) 338-344.

[5] Y. Chen, X. Feng, Y. Liu, X. Guan, C. Burda, L. Guo, Metal oxide-based tandem cells for self-biased photoelectrochemical water splitting, ACS Energy Letters, 5 (2020) 844-866.

[6] Z. Chen, H.N. Dinh, E. Miller, Photoelectrochemical water splitting, Springer, 2013.

[7] K. Shankar, J.I. Basham, N.K. Allam, O.K. Varghese, G.K. Mor, X. Feng, M. Paulose, J.A. Seabold, K.-S. Choi, C.A. Grimes, Recent advances in the use of TiO2 nanotube and nanowire arrays for oxidative photoelectrochemistry, The Journal of Physical Chemistry C, 113 (2009) 6327-6359.

[8] P. Qiu, F. Li, H. Zhang, S. Wang, Z. Jiang, Y. Chen, Photoelectrochemical performance of α-Fe2O3@ NiOOH fabricated with facile photo-assisted electrodeposition method, Electrochimica Acta, 358 (2020) 136847.

[9] H. Ennaceri, M. Boujnah, D. Erfurt, J. Rappich, X. Lifei, A. Khaldoun, A. Benyoussef, A. Ennaoui, A. Taleb, Influence of stress on the photocatalytic properties of sprayed ZnO thin films, Solar Energy Materials and Solar Cells, 201 (2019) 110058.

[10] Y. Qiu, S.-F. Leung, Q. Zhang, B. Hua, Q. Lin, Z. Wei, K.-H. Tsui, Y. Zhang, S. Yang, Z. Fan, Efficient photoelectrochemical water splitting with ultrathin films of hematite on three-dimensional nanophotonic structures, Nano letters, 14 (2014) 2123-2129.

[11] R. Pessoa, M. Fraga, L. Santos, M. Massi, H. Maciel, Nanostructured thin films based on TiO2 and/or SiC for use in photoelectrochemical cells: A review of the material characteristics, synthesis and recent applications, Materials Science in Semiconductor Processing, 29 (2015) 56-68.

[12] A.Y. Faid, N.K. Allam, Stable solar-driven water splitting by anodic ZnO nanotubular semiconducting photoanodes, RSC Advances, 6 (2016) 80221-80225.

[13] M. Khelladi, L. Mentar, A. Beniaiche, L. Makhloufi, A. Azizi, A study on electrodeposited zinc oxide nanostructures, Journal of Materials Science: Materials in Electronics, 24 (2013) 153-159.

[14] C. Klingshirn, ZnO: material, physics and applications, ChemPhysChem, 8 (2007) 782-803.

[15] D. Commandeur, G. Brown, E. Hills, J. Spencer, Q. Chen, Defect-rich ZnO nanorod arrays for efficient solar water splitting, ACS Applied Nano Materials, 2 (2019) 1570-1578.

[16] F. Kayaci, S. Vempati, I. Donmez, N. Biyikli, T. Uyar, Role of zinc interstitials and oxygen vacancies of ZnO in photocatalysis: a bottom-up approach to control defect density, Nanoscale, 6 (2014) 10224-10234.

[17] S.-F. Duan, Y.-F. Ji, W. Wang, D.-F. Han, H.-Y. Wang, Q.-Y. Wei, C.-F. Li, F. Jia, D.-X. Han, L. Niu, Unraveling the Impact of Electrochemically Created Oxygen Vacancies on the Performance of ZnO Nanowire Photoanodes, ACS Sustainable Chemistry & Engineering, 7 (2019) 18165-18173.

[18] J. Wang, R. Chen, L. Xiang, S. Komarneni, Synthesis, properties and applications of ZnO nanomaterials with oxygen vacancies: a review, Ceramics International, 44 (2018) 7357-7377.

[19] T. Xia, P. Wallenmeyer, A. Anderson, J. Murowchick, L. Liu, X. Chen, Hydrogenated black ZnO nanoparticles with enhanced photocatalytic performance, RSC advances, 4 (2014) 41654-41658.

[20] C. Wang, D. Wu, P. Wang, Y. Ao, J. Hou, J. Qian, Effect of oxygen vacancy on enhanced photocatalytic activity of reduced ZnO nanorod arrays, Applied Surface Science, 325 (2015) 112-116.

[21] V. Kumar, M. Gohain, R. Kant, O. Ntwaeaborwa, P. Hari, H. Swart, V. Dutta, Annealing induced oxygen defects on green sonochemically synthesized ZnO nanoparticles for photoelectrochemical water splitting, ChemistrySelect, 3 (2018) 11914-11921.

[22] H. Khan, S. Samanta, M. Seth, S. Jana, Role of Oxygen Defects on Photoelectrochemical Activity of ZnO Nanorods Grown on Transparent Conducting Oxide Thin Film, General Chemistry, 6 (2020) 190025.

[23] P. Camarda, F. Messina, L. Vaccaro, S. Agnello, G. Buscarino, R. Schneider, R. Popescu, D. Gerthsen, R. Lorenzi, F.M. Gelardi, Luminescence mechanisms of defective ZnO nanoparticles, Physical Chemistry Chemical Physics, 18 (2016) 16237-16244.

[24] A. Mohamedkhair, Q. Drmosh, M. Qamar, Z. Yamani, Nanostructured Magnéli-Phase W18O49 Thin Films for Photoelectrochemical Water Splitting, Catalysts, 10 (2020) 526.

[25] S.B. Kale, A. Lokhande, R. Pujari, C. Lokhande, Effect of pretreatment on catalytic activity of cobalt sulfide thin film for oxygen evolution reaction, Materials Letters, 228 (2018) 418-420.

[26] R. Rai, Analysis of the Urbach tails in absorption spectra of undoped ZnO thin films, Journal of Applied Physics, 113 (2013) 153508.

[27] C. Ton-That, M. Foley, M.R. Phillips, Luminescent properties of ZnO nanowires and as-grown ensembles, Nanotechnology, 19 (2008) 415606.

[28] C. Ton-That, L. Weston, M. Phillips, Characteristics of point defects in the green luminescence from Zn-and O-rich ZnO, Physical Review B, 86 (2012) 115205.

[29] S. Anantachaisilp, S.M. Smith, C. Ton-That, S. Pornsuwan, A.R. Moon, C. Nenstiel, A. Hoffmann, M.R. Phillips, Nature of red luminescence in oxygen treated hydrothermally grown zinc oxide nanorods, Journal of Luminescence, 168 (2015) 20-25.

[30] A. Janotti, C.G. Van de Walle, Fundamentals of zinc oxide as a semiconductor, Reports on progress in physics, 72 (2009) 126501.

[31] M. Foley, C. Ton-That, M.R. Phillips, Cathodoluminescence inhomogeneity in ZnO nanorods, Appl. Phys. Lett., 93 (2008) 243104.

[32] G. Li, T. Hu, G. Pan, T. Yan, X. Gao, H. Zhu, Morphology− function relationship of ZnO: polar planes, oxygen vacancies, and activity, The Journal of Physical Chemistry C, 112 (2008) 11859-11864.

[33] T.J. Penfold, J. Szlachetko, F.G. Santomauro, A. Britz, W. Gawelda, G. Doumy, A.M. March, S.H. Southworth, J. Rittmann, R. Abela, Revealing hole trapping in zinc oxide nanoparticles by time-resolved X-ray spectroscopy, Nature Communications, 9 (2018) 1-9.

[34] X. Wei, B. Man, M. Liu, C. Xue, H. Zhuang, C. Yang, Blue luminescent centers and microstructural evaluation by XPS and Raman in ZnO thin films annealed in vacuum, N2 and O2, Physica B: Condensed Matter, 388 (2007) 145-152.

[35] Y. Ling, G. Wang, D.A. Wheeler, J.Z. Zhang, Y. Li, Sn-doped hematite nanostructures for photoelectrochemical water splitting, Nano letters, 11 (2011) 2119-2125.

[36] E.S. Cho, M.J. Kang, Y.S. Kang, Enhanced photocurrent density of hematite thin films on FTO substrates: effect of post-annealing temperature, Physical Chemistry Chemical Physics, 17 (2015) 16145-16150.

[37] Y. Huang, Y. Yu, Y. Yu, B. Zhang, Oxygen vacancy engineering in photocatalysis, Solar RRL, 4 (2020) 2000037.

[38] P.M. Wojcik, L.D. Bastatas, N. Rajabi, P.V. Bakharev, D.N. McIlroy, The effects of sub-bandgap transitions and the defect density of states on the photocurrent response of a single ZnO-coated silica nanospring, Nanotechnology, 32 (2020) 035202.

[39] Y. Lee, S. Kim, S.Y. Jeong, S. Seo, C. Kim, H. Yoon, H.W. Jang, S. Lee, Surface-Modified Co-doped ZnO photoanode for photoelectrochemical oxidation of glycerol, Catalysis Today, 359 (2021) 43-49.

[40] H. Li, X. Li, W. Dong, J. Xi, G. Du, Z. Ji, Cu nanoparticles hybridized with ZnO thin film for enhanced photoelectrochemical oxygen evolution, Journal of Alloys and Compounds, 768 (2018) 830-837.

[41] H.R. Khan, M. Aamir, B. Akram, A.A. Tahir, M.A. Malik, M.A. Choudhary, J. Akhtar, Superior visible-light assisted water splitting performance by Fe incorporated ZnO photoanodes, Materials Research Bulletin, 122 (2020) 110627.

[42] F.S. Lim, S.T. Tan, Y. Zhu, J.-W. Chen, B. Wu, H. Yu, J.-M. Kim, R.T. Ginting, K.S. Lau, C.H. Chia, Tunable plasmon-induced charge transport and photon absorption of bimetallic Au–Ag nanoparticles on ZnO photoanode for photoelectrochemical enhancement under visible light, The Journal of Physical Chemistry C, 124 (2020) 14105-14117.

[43] D. Maity, K. Karmakar, D. Pal, S. Saha, G.G. Khan, K. Mandal, One-Dimensional p-ZnCo2O4/n-ZnO Nanoheterojunction Photoanode Enabling Photoelectrochemical Water Splitting, ACS Applied Energy Materials, 4 (2021) 11599-11608.

[44] P. Vairale, V. Sharma, B. Bade, A. Waghmare, P. Shinde, A. Punde, V. Doiphode, R. Aher, P. Subhash, S. Nair, Melanin sensitized nanostructured ZnO photoanodes for efficient photoelectrochemical splitting of water: synthesis and characterization, Engineered Science, 11 (2020) 76-84.

[45] X. Long, T. Wang, J. Jin, X. Zhao, J. Ma, The enhanced water splitting activity of a ZnO-based photoanode by modification with self-doped lanthanum ferrite, Nanoscale, 13 (2021) 11215-11222.

[46] J. Han, H. Xing, Q. Song, H. Yan, J. Kang, Y. Guo, Z. Liu, A ZnO@ CuO core–shell heterojunction photoanode modified with ZnFe-LDH for efficient and stable photoelectrochemical performance, Dalton Transactions, 50 (2021) 4593-4603.

[47] P. Sahoo, A. Sharma, S. Padhan, R. Thangavel, Visible light driven photosplitting of water using one dimensional Mg doped ZnO nanorod arrays, International Journal of Hydrogen Energy, 45 (2020) 22576-22588.

[48] Y. Lin, S. Liu, Robust ZnO nanowire photoanodes with oxygen vacancies for efficient photoelectrochemical cathodic protection, Applied Surface Science, 566 (2021) 150694.

[49] K. Govatsi, G. Syrrokostas, S. Yannopoulos, S. Neophytides, Optimization of aluminum doped ZnO nanowires for photoelectrochemical water splitting, Electrochimica Acta, 392 (2021) 138995.

[50] I.V. Bagal, S. Jun, M. Choi, A. Abdullah, A. Waseem, S. Ahn, M.A. Kulkarni, Y.-H. Cho, S.-W. Ryu, Investigation of charge carrier dynamics in beaded ZnO nanowire decorated with SnS2/IrOx cocatalysts for enhanced photoelectrochemical water splitting, Applied Surface Science, 613 (2022) 156091.